

Computational study on aerodynamically coupled piezoelectric harvesters

Bruno A Roccia^{1,2} , Marcos L Verstraete¹, Luis R Ceballos¹ , Balakumar Balachandran³ and Sergio Preidikman²

Journal of Intelligent Material Systems and Structures

1–16

© The Author(s) 2020

Article reuse guidelines:

sagepub.com/journals-permissions

DOI: 10.1177/1045389X20930093

journals.sagepub.com/home/jim



Abstract

In this work, the authors present a two-dimensional computational model for predicting the aeroelastic response as well as the output power of vertically arranged harvesters by taking into account all aerodynamic interactions. The piezo-aeroelastic framework consists of the following: (1) an aerodynamic model based on the unsteady vortex-lattice method to compute the aerodynamic forces; (2) a discrete parameter model for each harvester with 3 degrees of freedom (plunge motion, pitch motion, and the voltage generated by the piezoelectric effect); (3) an inter-model connection to exchange information between models at each time step; and (4) a numerical scheme based on the Hamming's fourth-order predictor–corrector method to integrate all the governing equations in the time domain. The results obtained allow us to infer new insights into the flutter onset as well as the post-critical behavior of harvester arrangements. An interesting finding is that the flutter speed is significantly decreased as the distance between the harvesters is reduced. The results suggest the strong possibility of effective energy extraction at low flow speeds using properly distributed harvester arrangements. However, in post-critical conditions, the output power is significantly enhanced as the free-stream speed is increased.

Keywords

energy harvesting, aeroelastic flutter, unsteady aerodynamics, piezoelectricity, array of harvesters

1. Introduction

A flexible body immersed in a fluid flow can experience oscillations as a consequence of interactions between inertial, elastic, and aerodynamic forces (Hodges and Pierce, 2011). Among the different aeroelastic phenomena, flutter has been extensively studied over several decades, as this instability has been a key for many catastrophic accidents in aeronautical and civil structures. Recently, the scientific community has envisaged the possibility of using this nonlinear phenomenon as a desirable means for electric energy generation (Rostami and Armandei, 2017). From an energy transduction viewpoint, one way to exploit this aeroelastic mechanism is to consider flexible structures integrated with piezoelectric layers, thus allowing the transformation of self-sustained mechanical vibrations (induced during a critical or post-critical flutter scenario) into an electrical charge (through the direct piezoelectric effect).

Since the end of the 2000s, several efforts have been published on energy harvesting based on aeroelastic flutter (EHAF) (Bryant and Garcia, 2009; Dias et al., 2014; Doare and Michelin, 2011; Erturk et al., 2010).

Although, through these studies, one can obtain new insights on the linear flutter speed behavior and design of harvester devices, the risk and potential of energy harvesting with wing-based aeroelastic systems can be best assessed through nonlinear analysis (Bae and Inman, 2014; Wu et al., 2017). The nonlinear response of a flutter-based aeroelastic system is generally influenced by a combination of nonlinearities (structural, geometric, inertia, freeplay, damping, and/or aerodynamic) making the associated analysis complex and computationally expensive compared to linear analysis. In Table 1, the authors present a summary of the

¹Group of Applied Mathematics, Engineering School, National University of Rio Cuarto, Rio Cuarto, Argentina

²Institute of Advanced Studies in Engineering and Technology (IDIT) UNC-CONICET and Department of Structures, F.C.E.F. y N., National University of Córdoba, Córdoba, Argentina

³University of Maryland, College Park, MD, USA

Corresponding author:

Bruno A Roccia, Group of Applied Mathematics, National University of Rio Cuarto, Rio Cuarto 5800, Córdoba, Argentina.

Email: bruno.roccia@gmail.com

Table 1. Different aeroelastic models used for flutter-based energy harvesting.

Author	Aerodynamic model	Structural model	Power output	Main goal
Bryant and Garcia (2009)	Peter's theory	Linear spring	2.0 mW	Novel energy harvesting device driven by aeroelastic flutter
Bryant et al. (2010)	Semi-empirical, nonlinear, and unsteady model Peters (1985)	Linear spring	2.2 mW	Energy harvesting for a helicopter rotor blade
Erturk et al. (2010)	Theodorsen's theory	Linear spring	10.7 mW	Mathematical modeling and experimental validation of a piezo-aeroelastic airfoil
Sousa et al. (2011)	Generalized Theodorsen's theory	Nonlinear	28.6 mW	Linear and nonlinear modeling of a 2-DOF piezo-aeroelastic (pitch nonlinearity)
Wu et al. (2017)	ONERA dynamic stall model	Linear spring	6.3 W	Power output analysis of an energy harvester based on an airfoil with double plunge degrees of freedom
Elahi et al. (2019)	Theodorsen's theory	Nonlinear	0.55 mW	Evaluation of a piezoelectric aeroelastic energy harvester based on the limit cycle oscillation phenomenon (considering freeplay)
Bao et al. (2019)	Unsteady model based on Leishman–Beddoes theory	Linear	0.3233 W	Output power analysis of a beam (with a piezoelectric patch stick to it) fixed to the trailing edge of a typical airfoil section
Current	Unsteady vortex-lattice method (2D)	Linear	0.12609 W	Flutter onset investigation for two vertically distributed harvesters

DOF: degree-of-freedom.

numerical models available in the literature to study the piezo-aeroelastic behavior of flutter-based energy harvesters. Despite the progress made, most studies in the literature highlight the low amount of energy produced by aeroelastic harvesters; a fact that has driven researchers to different proposals to make this technology sustainable, such as the idea of using different harvester arrangements to enhance the power output. In this direction, the work of Bryant et al. (2012) has provided new insights on how aerodynamic interferences affect the efficiency of harvester arrays. Specifically, they showed that the wake interaction among harvesters considerably affects the vibration amplitude, frequency, and power output of the trailing devices. Deivasigamani et al. (2014) led an experimental study of an array of two harvesters. From the results, one can glean that when the harvesters are placed along the wind direction, the downstream harvester provides 20%–40% more power when compared with a stand-alone configuration. With the aim to understand the underlying physics behind this phenomenon, McCarthy et al. (2014) led a qualitative and quantitative experimental investigation for two piezoelectric energy harvesters placed in tandem. Through a flow visualization and voltage data analysis, they found that the leading-edge vortex (LEV) shed by the upstream harvester does not affect the downstream harvester. However, the trailing

edge vortices generated by the upstream harvester act to increase the maximum tip speed of the harvester behind it, which consequently amplifies the power generated by the downstream piezoelectric airfoil.

Despite the pioneering studies, the integration of several harvesters as a possible technological solution involves a large number of challenges, among which, the dependence of the output power on the spatial distribution of harvesters (because of the aerodynamic interference) remains a poorly understood topic (McCarthy et al., 2016). Here, the authors investigate how the separation between two harvesters (in a vertical configuration) affects the flutter onset and the output electric power. For this purpose, a numerical framework well suited for studying the piezo-aeroelastic behavior of harvester arrays has been developed. The entire system under study is partitioned in two subsystems (the piezoelectric model and the aerodynamic model) between which one can exchange information in a bi-directional way. The piezoelectric model is similar to that used by Erturk et al. (2010), which is based on a 3-degree-of-freedom (3-DOF) discrete parameter approach (plunge, pitch, and voltage across the resistive load). The loads coming from the flow field around the harvester array are predicted using a two-dimensional (2D) version of the well-known unsteady vortex-lattice method (UVLM). Finally, the set of ordinary differential equations (ODEs) is integrated simultaneously

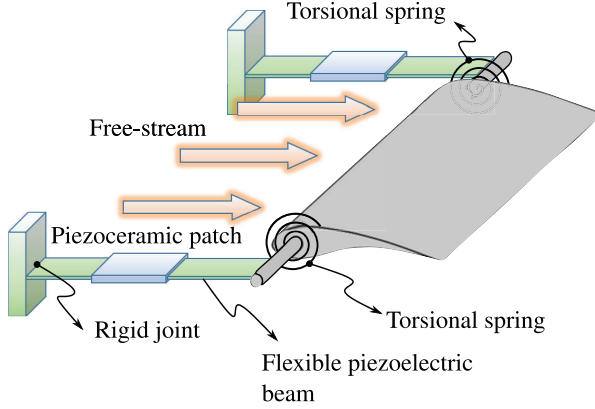


Figure 1. Scheme of a single piezo-aeroelastic harvester. Source: Adapted from Erturk et al. (2010).

in the time domain by means of the Hamming's fourth-order scheme (Preidikman and Mook, 2000).

The rest of this article is organized as follows. In section 2, the discrete parameter formulation for a piezoelectric airfoil is presented. This is followed by section 3, which presents a brief description of the UVLM adopted to account for the aerodynamic loads. In section 4, the simulation strategy along with the integration scheme to solve the resulting ODEs is presented. In section 5, the numerical framework is validated by comparing results against experimental data. In addition, results concerning the flutter onset and power output for an array of harvesters are investigated and discussed. Finally, to close the article, concluding remarks and thoughts of future works are collected together in section 6.

2. Piezoelectric model

In this section, the authors describe the computational model used to study the nonlinear electro-aeroelastic behavior of an array of harvesters. Previously, Erturk et al. (2010) developed an experimental and analytical model intended for quantifying the electrical power produced at the flutter boundary of a single piezo-aeroelastic airfoil. Here, this configuration is extended to multiple airfoils. In the single piezo-aeroelastic model, there is a thin, symmetrical, rigid, large aspect ratio wing linked, through torsional springs, to a supporting piezoelectric structure responsible for transforming mechanical vibrations into electrical energy (see Figure 1).

A correct numerical model of the physical system presented in Figure 1 must necessarily involve the following: (1) an aerodynamic model, with the capability for estimation of loads coming from the surrounding fluid; (2) a structural model for predicting the consistent response of the mechanical system under excitation of the acting loads; and (3) a technique for transferring

information between the aerodynamic and structural models, where, in the most general case, the grids can be very different in nature. Although, in this work, the harvesters are not structurally linked to each other, they are weakly coupled through the aerodynamics. In fact, this aerodynamic interference phenomenon ultimately determines the main aeroelastic characteristics of the entire dynamic system, such as the flutter onset velocity for the system. The substantial “deformation” of each harvester induces significant changes in the overall flow pattern around them and, therefore, the aerodynamic loads, which in turn induce further changes in the configuration of the piezoelectric system. This feedback between the aerodynamics and the movement of the harvesters (flow field boundaries) generates a strong coupling between the flow and structural models. In order to capture these complex interactions with a numerical model, in this work, the authors have chosen a two-way non-monolithic coupling method strategy (Preidikman et al., 2017; Roccia et al., 2017).

Erturk et al. (2010) represented the physical system shown in Figure 1 using a lumped-parameter model in which the harvester is idealized as a 2D airfoil (see Figure 2). Under these assumptions, the configuration space for one harvester can be described by $\chi_i = \mathbb{R}^2 \times SO(2)$, where $SO(2)$ is the special orthogonal group in two dimensions. In this work, the configuration coordinate vector $\mathbf{q}_i(t) \in \chi_i$ is given by

$$\mathbf{q}_i(t) = (h(t), \theta(t), V(t))^T \quad (1)$$

where $h(t)$ is the plunge displacement (translation), $\theta(t)$ is the pitch angle, and $V(t)$ is the voltage generated. Due to the lack of constraint equations in the system, the number of degrees of freedom n_{DOFs} for each piezoelectric airfoil is equal to the dimension of the configuration space, $n_{DOFs} = \dim(\chi_i) = 3$.

According to Erturk et al. (2010), the piezoelectric model is introduced into the dynamic system by coupling the plunge displacement and the electrical variables through an electromechanical constant, denoted as λ . The piezo-aeroelastic equations of the system presented in Figure 2 are obtained by modifying the linear aeroelastic equations of a typical section (Hodges and Pierce 2011). Following the same procedure as in prior studies (Bryant and Garcia, 2011; Erturk et al., 2010), the equations of motion (EoMs) for one piezo-aeroelastic harvester are obtained in matrix form as

$$\begin{bmatrix} m + m_f & mx_\theta b & 0 \\ mx_\theta b & I_p & 0 \\ 0 & 0 & 0 \end{bmatrix} \ddot{\mathbf{q}}_i(t) + \begin{bmatrix} d_h & 0 & 0 \\ 0 & d_\theta & 0 \\ \lambda & 0 & C^{eq} \end{bmatrix} \dot{\mathbf{q}}_i(t) + \begin{bmatrix} k_h & 0 & -\frac{\lambda}{l} \\ 0 & k_\theta & 0 \\ 0 & 0 & \frac{1}{R} \end{bmatrix} \mathbf{q}_i(t) = \begin{Bmatrix} L \\ M \\ 0 \end{Bmatrix} \quad (2)$$

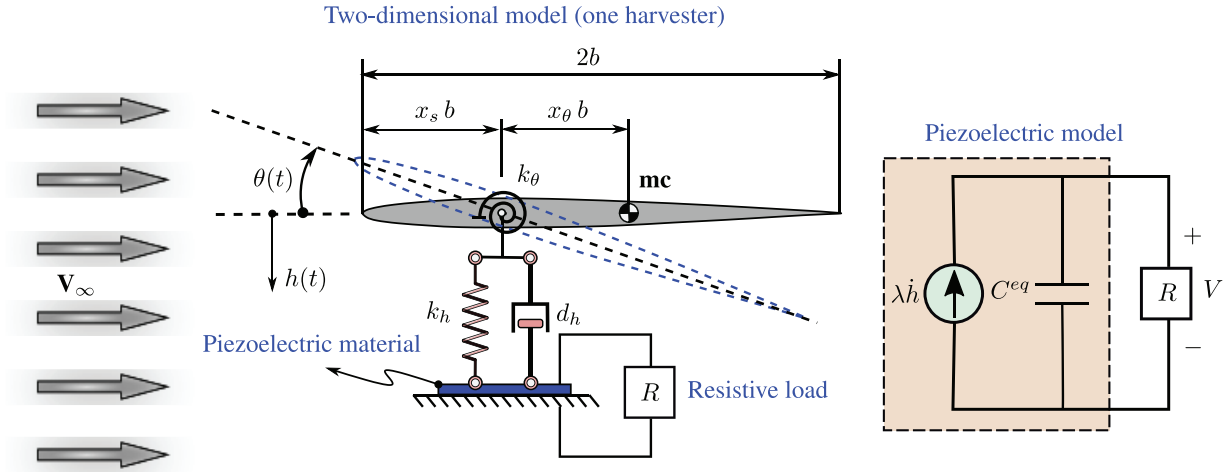


Figure 2. Piezo-aeroelastic section scheme under uniform airflow used in the current work.

where m is the airfoil mass per length, m_f accounts for the fixture mass per length in the experiments connecting the airfoil to the plunge springs ($m_f = 0$ for the ideal representation given in Figure 2), I_p is the moment of inertia per length about the reference point (spring joints), b is the semichord length, l is the span length, x_θ is the dimensionless chordwise offset of the reference point from mass center (MC), k_h (k_θ) is the stiffness per length in the plunge DOF (pitch DOF), L is the aerodynamic lift per length, M is the aerodynamic pitching moment per length, d_h (d_θ) is the structural damping coefficients in the plunge DOF (pitch DOF), R is the load resistance, V is the voltage across the resistive load, C^{eq} is the equivalent capacitance of the piezoceramic layers, λ is the electromechanical coupling term, and the overdot represents the differentiation with respect to time.

The ODEs (2) govern the time evolution of one piezo-aeroelastic airfoil. In order to consider an array of harvesters (see Figure 3), the ODEs in equation (2) are recast as

$$\mathbf{M}_i \ddot{\mathbf{q}}_i(t) + \mathbf{C}_i \dot{\mathbf{q}}_i(t) + \mathbf{K}_i \mathbf{q}_i(t) = \mathbf{F}_i \quad (3)$$

where \mathbf{M}_i , \mathbf{C}_i , \mathbf{K}_i , and \mathbf{F}_i are the mass matrix, damping matrix, stiffness matrix, and the external load vector for the i th harvester, respectively. It should be noted that here, only the aerodynamic forces are included in \mathbf{F}_i .

Finally, the EoMs for the complete dynamic system shown in Figure 3 are obtained by assembling the EoMs for each harvester as

$$\mathbf{M} \ddot{\mathbf{q}}(t) + \mathbf{C} \dot{\mathbf{q}}(t) + \mathbf{K} \mathbf{q}(t) = \mathbf{F} \quad (4)$$

where $\mathbf{M} \in \mathbb{R}^{3n \times 3n}$ is the global mass matrix, $\mathbf{C} \in \mathbb{R}^{3n \times 3n}$ is the global damping matrix, $\mathbf{K} \in \mathbb{R}^{3n \times 3n}$ is the global stiffness matrix, $\mathbf{F} \in \mathbb{R}^{3n \times 1}$ is the global load vector, $\mathbf{q} \in \mathbb{R}^{3n \times 1}$ is the global vector of generalized coordinates, and n is the number of harvesters in the wind energy system.

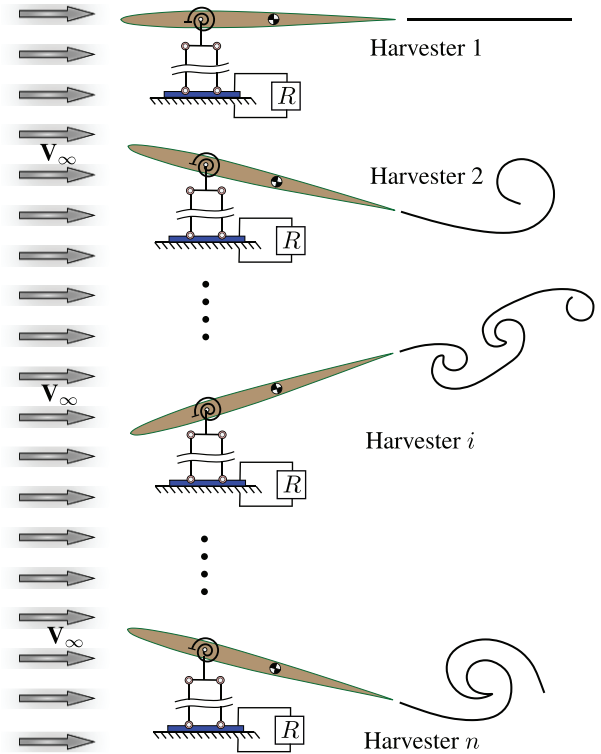


Figure 3. Conceptual scheme of an array of aeroelastic harvesters.

Due to the uncoupled nature of the system, from a piezoelectric point of view, \mathbf{M} , \mathbf{C} , and \mathbf{K} are in block diagonal forms. The set of ODEs is only coupled through the aerodynamic forces, which are included on the right-hand side, namely, \mathbf{F} .

3. Aerodynamic model

As the main goal of this work is to study the aeroelastic behavior of a set of harvesters when they are close to

each other, the authors must necessarily implement an unsteady aerodynamic model capable of capturing the aerodynamic interference among them. In other words, a fluid model able to accurately estimate the aerodynamic loads and their variation as a consequence of the fluctuations in the flow pattern triggered by neighboring harvesters. Thus, the vector \mathbf{F} , which is a collection of the forces acting on the n piezoelectric airfoils, depends on the movement of the entire harvesters' array.

On this basis, the authors have adopted a 2D version of the well-known UVLM to compute the aerodynamic loads. Currently, the utilization of UVLMs has been gaining ground in the study of unsteady problems, in which free-wake methods are mandatory because of the geometric complexity of the mechanical or aeronautical system under analysis. This method can be applied to 2D or three-dimensional (3D) flows around lifting and nonlifting surfaces. It is general in the sense that bodies may undergo any time-dependent deformation as well as execute any maneuver in the space surrounded by moving air (Fitzgerald et al., 2011; Konstadinopoulos et al., 1981; Preidikman, 1998; Roccia et al., 2013). The flow around the bodies, that is, each piezoelectric airfoil, is assumed to be inviscid, incompressible, and irrotational over the entire flow field, except at the solid boundaries and wakes. A significant advantage of the UVLM is the desirable trade-off between a relatively high precision (in terms of capturing all possible aerodynamic interferences) and a moderate computational

cost when compared to flow solvers based on computational fluid dynamics (CFD) techniques.

The bound-vortex sheet represents the boundary layer on the surface of the body, and its position is specified. For the case of thin wings, the vortex sheets on the upper and lower surfaces are merged into a single surface along the camber line. However, the positions of the free-vortex sheets representing the wakes are not specified a priori; they are allowed to deform freely until they assume force-free positions as determined by the solution. The two types of vortex sheets are joined along the sharp edges where separation occurs (here only the trailing edge).

Vortex methods are based on the spatial discretization of the continuous vortex sheets into straight elements of concentrated vorticity. As a consequence, the vorticity of each element has associated with it a single point vortex (denoted as vortex point, VP) whose circulation is such that the non-penetration condition is satisfied at the so-called control points (CPs) (see Figure 4).

Outside of the wakes and boundary layers, the spatial-temporal evolution of the velocity potential $\Psi(\mathbf{r}; t)$ is governed by the well-established Laplace equation (Katz and Plotkin, 2001), which is complemented by a set of boundary conditions. For a body immersed in a flow, the normal component of the velocity of all fluid particles relative to the body surface must be zero on the body surface (no-penetration condition). This condition is imposed on the CPs located at $3/4$ of the j th aerodynamic element, c_j (see Figure 4).

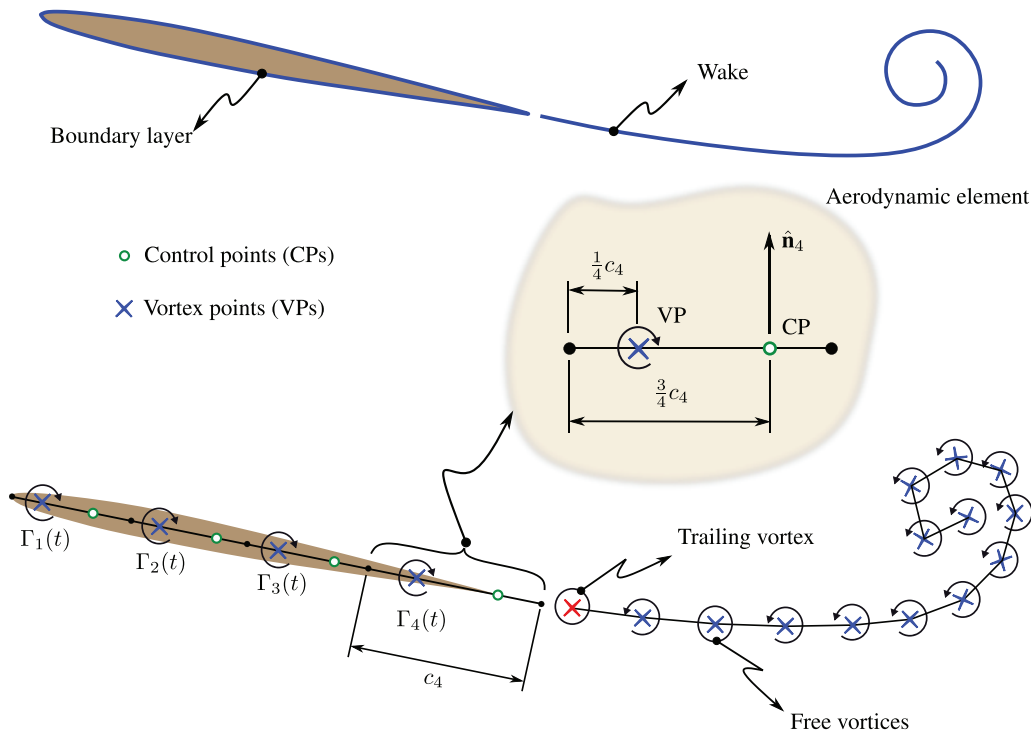


Figure 4. Discretization of bounded-vortex sheets and free-vortex sheets.

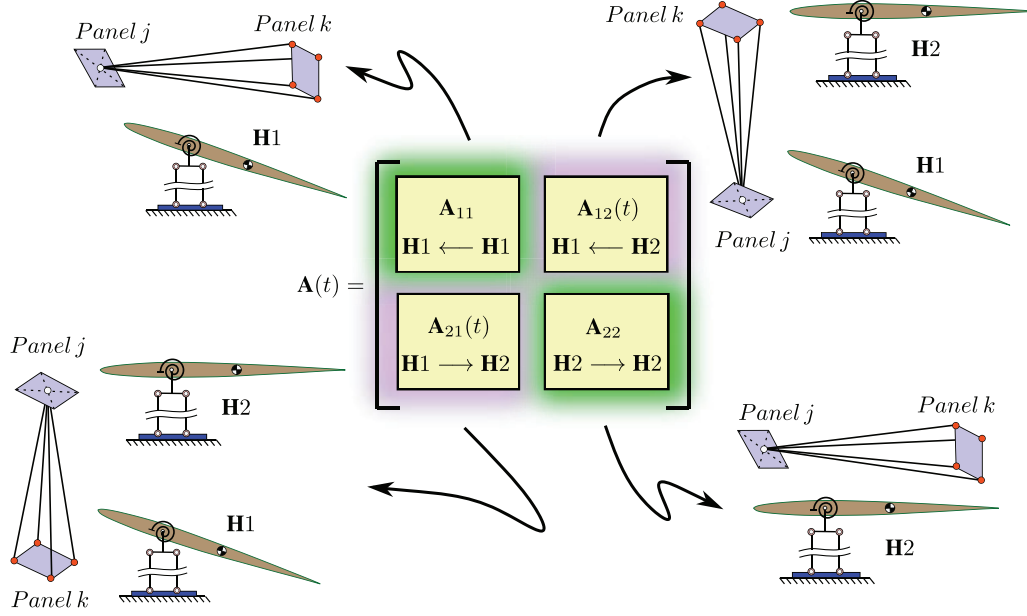


Figure 5. Identification of aerodynamic influence coefficient submatrices of $\mathbf{A}(t)$ for two harvesters.

Another boundary condition, called regularity at infinity, requires that all disturbances due to a moving body in a fluid decay away from it and its wakes. In addition, since the flow is inviscid, the Kelvin's circulation theorem requires that the total circulation around a closed fluid path at every instant enclosing the airfoil and its wakes remain constant in time.

The imposition of the no-penetration condition at each CP along with Kelvin's circulation theorem leads to the following set of linear algebraic equations for the harvester system

$$\begin{aligned} \sum_{k=1}^{n(N+1)} a_{jk}(t) \Gamma_k(t) &= -(\mathbf{V}_\infty + \mathbf{V}_W^j - \mathbf{V}_P^j) \cdot \hat{\mathbf{n}}_j \\ \text{for } j &= 1, 2, \dots, n(N+1) - 1n \\ \sum_{k=1}^{n(N+1)} b_{jk} \Gamma_k(t) &= \sum_{k=1}^{n(N+1)} b_{jk} \Gamma_k(t - \Delta t) \\ \text{for } j &= nN + 1, \dots, n(N+1) \end{aligned} \quad (5)$$

the b_{jk} are the components of a $n \times n(N+1)$ boolean submatrix which allows satisfying the Kelvin's circulation theorem for each harvester where $a_{jk}(t)$ is the influence aerodynamic coefficients, Γ_k is the circulation of the VP belonging to the k th aerodynamic element, \mathbf{V}_∞ is the free-stream velocity, \mathbf{V}_W^j is the velocity at the CP j due to the free vortices (wake), \mathbf{V}_P^j is the velocity of the solid at the CP j , $\hat{\mathbf{n}}_j$ is the unit vector normal to the body surface at CP j , and N is the number of aerodynamic elements per harvester. From the solution of the system (5), one obtains the circulations Γ_k associated with all of the aerodynamic elements making up the array of harvesters, as well as, all those vortices located at the trailing edges, $\Gamma_{nN+1}, \dots, \Gamma_{n(N+1)}$.

Due to the possibility of multiple harvesters, the aerodynamic influence matrix, $\mathbf{A}(t)$, can be split into different submatrices according to the following: (1) the influence between aerodynamic elements belonging to the same harvester, and (2) the influence between aerodynamic elements belonging to different harvesters (see Figure 5). The former leads to block matrices located on the main diagonal, while the latter leads to out-of-diagonal blocks. The submatrices located on the main diagonal need to be only updated at each time step if the relative positions between aerodynamic elements change (i.e. they are allowed to deform). Here, the piezoelectric airfoils are modeled as rigid bodies; therefore, such submatrices do not need to be re-evaluated. On the contrary, the out-of-diagonal blocks need to be updated at each time step because the relative positions between harvesters change with time.

The velocity field in any point of the space is given by the Biot-Savart law, which for 2D flows can be expressed as follows

$$\mathbf{V}(\mathbf{r}; t) = \frac{1}{2\pi} \iint_{S(\mathbf{r}_0; t)} \frac{\boldsymbol{\Omega}(\mathbf{r}_0; t) \times (\mathbf{r} - \mathbf{r}_0)}{r^2} dS(\mathbf{r}_0) + \mathbf{V}_\infty \quad (6)$$

where $S(\mathbf{r}_0; t)$ is the flow domain region, \mathbf{r}_0 is the position vector of a point belonging to the flow domain region $S(\mathbf{r}_0; t)$, \mathbf{r} is the field point where the velocity is being computed, $r = \|\mathbf{r} - \mathbf{r}_0\|$ is the Euclidean distance between the VP and the evaluation point, and $\boldsymbol{\Omega}(\mathbf{r}_0; t)$ is the vorticity vector at \mathbf{r}_0 .

The integrand of equation (6) is zero wherever $\boldsymbol{\Omega}$ is null. Therefore, the regions where the flow is irrotational do not contribute at all to the velocity field \mathbf{V} . This fact allows to determine \mathbf{V} in both the viscous and

non-viscous regions through the vorticity distribution is in the viscous region only. For a 2D vortex, it can be shown that the velocity field given in equation (6) has a simple expression in polar coordinates (Katz and Plotkin, 2001), being $V_r = 0$ and $V_\theta = -\Gamma/2\pi r$, which in turn can be expressed in Cartesian coordinates as

$$\mathbf{V}(\mathbf{r}; t) = \frac{\Gamma}{2\pi r^2} \left\{ [(\mathbf{r} - \mathbf{r}_0) \cdot \hat{\mathbf{j}}] \hat{\mathbf{i}} - [(\mathbf{r} - \mathbf{r}_0) \cdot \hat{\mathbf{i}}] \hat{\mathbf{j}} \right\} \quad (7)$$

where $\hat{\mathbf{i}}$ and $\hat{\mathbf{j}}$ are the canonical unit vectors associated with the Cartesian coordinate lines x and y in \mathbb{R}^2 .

When the field point approaches the VP, \mathbf{V} as given in equation (7) presents a singularity at the core. Therefore, at a VP, equation (7) leads to an amplification of numerical discretization errors. Choices for regularizing this singularity include vortex-blob regularization, vortex-patch regularization, viscous regularization, and so on. In this work, the regularization proposed by Krasny (1987) is used to compute the influence of the vortices in the wakes upon one another and with the body surfaces.

3.1. Aerodynamic loads

The aerodynamics loads acting on the lifting surfaces are computed by the following three steps. First, the pressure jump coefficient is computed at each CP by integrating the unsteady Bernoulli equation (Preidikman, 1998; Roccia et al., 2013)

$$(\Delta C_p)_k = \frac{(V_U^2 - V_L^2)_k}{V_\infty^2} + \frac{2}{V_\infty^2} (\partial_t \Psi|_U - \partial_t \Psi|_L)_k \quad (8)$$

where V_∞ is the magnitude of the free-stream velocity vector, ∂_t denotes the partial time derivative, and the subscript U (L) stands for a point located above (below) the CP k .

The term $V_U^2 - V_L^2$ in equation (8) can be evaluated using the jump in the tangential velocity across the vortex sheet, $\Delta \mathbf{V}$, along with a “mean” velocity, \mathbf{V}_m , which does not recognize the presence of the local vorticity. The velocities on the upper and lower surfaces may be written as

$$\begin{aligned} \mathbf{V}_U &= \mathbf{V}_m + \frac{1}{2} \Delta \mathbf{V} \\ \mathbf{V}_L &= \mathbf{V}_m - \frac{1}{2} \Delta \mathbf{V} \end{aligned} \quad (9)$$

After using equation (9), the first term of equation (8) becomes

$$V_U^2 - V_L^2 = 2\mathbf{V}_m \cdot \Delta \mathbf{V} \quad (10)$$

The expression of $\Delta \mathbf{V}$ for an aerodynamic element k can be derived from the 3D formula given by Preidikman (1998) as

$$\Delta \mathbf{V}_k = \frac{\Gamma_k}{c_k} \hat{\mathbf{t}}_k \quad (11)$$

where $\hat{\mathbf{t}}_k$ is the tangential unit vector along the chordwise direction, and c_k is the length of the k th aerodynamic element.

The second term in equation (8) is derived from a multi-variable Taylor expansion of $\Psi(\mathbf{r}; t)$ around \mathbf{r} and t . Taking the limit for $\Delta t \rightarrow 0$ and considering a convenient choice for $\Delta \mathbf{r}$ (a point fixed either just below or just above a CP in the moving lattice), the velocity potential $\Psi(\mathbf{r}; t)$ becomes a function of t only. In this way, $\lim_{\Delta t \rightarrow 0} \Delta \mathbf{r} / \Delta t$ is the velocity of a point fixed to the airfoil (Preidikman, 1998). After some algebraic manipulations, $\partial_t \Psi$ can be expressed as

$$\partial_t \Psi(\mathbf{r}; t) = \frac{\mathcal{D}\Psi}{\mathcal{D}t} \Big|_P - \nabla \Psi(\mathbf{r}; t) \cdot \mathbf{V}_P \quad (12)$$

where $\mathcal{D}\Psi/\mathcal{D}t$ is the substantial derivative of $\Psi(\mathbf{r}; t)$ following a point fixed to the moving lattice (not a fluid particle as is usual for this term), and \mathbf{V}_P is the velocity of a point fixed to the lattice.

Then, equation (12) can be used to compute $\partial_t \Psi(\mathbf{r}_U; t) - \partial_t \Psi(\mathbf{r}_L; t)$ as follows

$$[\partial_t \Psi(\mathbf{r}_U; t) - \partial_t \Psi(\mathbf{r}_L; t)]_k = \frac{\mathcal{D}\Gamma_k}{\mathcal{D}t} - \Delta \mathbf{V}_k \cdot \mathbf{V}_k^{CP} \quad (13)$$

Here, $\Delta \mathbf{V}_k$ was defined in equation (11) and \mathbf{V}_k^{CP} is the velocity of the CP associated with the k th aerodynamic element. In this work, the numerical procedure used to compute the substantial derivative $\mathcal{D}\Gamma_k/\mathcal{D}t$ consists of a first-order backward finite-difference approximation

$$\frac{\mathcal{D}\Gamma_k(t)}{\mathcal{D}t} \simeq \frac{\Gamma_k(t) - \Gamma_k(t - \Delta t)}{\Delta t} \quad (14)$$

Then, the force on the k th aerodynamic element is computed as the product of the pressure jump times the element area times the normal unit vector located at the CP k . Finally, the resultant forces and moments are computed as the vector sum of the forces and their moments about a common point. For the i th harvester, the external load vector, \mathbf{F}_i , is given by

$$\mathbf{F}_i = \frac{1}{2} \rho_\infty V_\infty^2 \cos \theta_i \left(\sum_{k=1}^N (\Delta C_p)_k, - \sum_{k=1}^N (\Delta C_p)_k x_k, 0 \right)^T \quad (15)$$

where θ_i is the pitch angle of the i th harvester, ρ_∞ is the free-stream density, and x_k is the distance from the CP k to the reference point (here the spring joint).

Once the loads have been computed, each VP of the wakes is “convected” to its new position by means of the following approximated method

$$\mathbf{r}_{vp}(t + \Delta t) \approx \mathbf{r}_{vp}(t) + \mathbf{V}_{vp}(t)\Delta t \quad (16)$$

where \mathbf{r}_{vp} and \mathbf{V}_{vp} are the position and velocity of a VP belonging to the wakes (including the starting vortex), and Δt is the time step.

4. Simulation scheme

In the approach followed here, the authors treat the piezoelectric model (called Simulator 1) and the airflow model (called Simulator 2) as different subsystems of a single dynamical system. Between these two simulators, one can exchange information bi-directionally in an iterative sequence in order to continuously improve the estimation of the piezoelectric response and the aerodynamic loads, respectively. On one hand, the numerical scheme used by Simulator 2 is well-known and can be found in the literature (e.g. Konstadinopoulos et al., 1981; Preidikman et al., 2017; Roccia et al., 2013; Verstraete et al., 2015). On the other hand, the numerical procedure adopted for Simulator 1 to solve the EoMs of the harvester array is based on Hamming's fourth-order predictor-corrector method (Carnahan et al., 1969; Preidikman et al., 2017). This method requires that the set of second-order differential equations presented in equation (4) to be re-written as a first-order system of ODEs.

In this work, the wing associated with each piezoelectric airfoil is considered as being rigid. This assumption simplifies the exchange of information between models. On one hand, the forces coming from the aerodynamics (on each CP) are transferred to the reference point using simply mechanical considerations. On the other hand, the displacements and velocities resulting from the numerical integration of the EoMs are transferred to the aerodynamic grid using simply rigid body kinematics.

On this basis, during a time step Δt , the wakes are consistently convected to their new positions with the requirement that vorticity moves with the fluid particles, while, simultaneously, all the piezoelectric airfoils of the harvester array move to their new position as a result of the acting forces. This concept is implemented by performing the following sequence of steps to calculate the solution at time $t + \Delta t$ as follows:

1. Simulator 2 is used to convect the wakes to their new positions. A fluid particle in the wake moves from its current position $\mathbf{r}_{vp}(t)$ to its new position $\mathbf{r}_{vp}(t + \Delta t)$ according to equation (16). During the rest of the procedure for this time step, the wake is frozen.
2. With the current loads computed by Simulator 2, Simulator 1 is used to predict the response of each harvester in the array.
3. The current state of the harvester array is used as input to Simulator 2 and the loads are

recalculated, but as stated above, the wake remains frozen. Then, these loads are used as input to Simulator 1 and the state of the harvesters is updated. This step is repeated until convergence. Usually, three to four iterations are required to reduce the error to be less than 10^{-10} .

4. Then, the final position and velocity of the harvester array are evaluated using Simulator 1, and these values are used by Simulator 2 to recalculate the flow field and obtain the final estimate for the aerodynamic loads.

Although the flow and piezoelectric solvers are computational implementations of physical fields independently modeled, the coupling procedure is indeed strong because information is bi-directionally exchanged, and the chosen step, which advances the solution in time, is unique for both simulation environments (see Figure 6).

5. Numerical results

In this section, the authors present some numerical results obtained from the implementation in Fortran 90 of the proposed methodology. Since the most expensive part of the simulation process is associated with the aerodynamic simulator, specifically the wake convection, the code has been explicitly parallelized using a model of shared memory architecture. The parallelization strategy consists in performing a domain decomposition centered on the input data. Its computational implementation was performed using an OpenMP* library.

For all cases, the code was run on a desktop computer with an Intel® Core™ i9-7980XE extreme edition processor, RAM DDR4 2666 MHz of 32 GB CL18, and a hard disk SATA 3 (6.0 Gb/s, 7200 r/min) Western Digital Black of 2 TB. The results obtained using the current numerical tool are compared against the analytical and experimental data reported by Erturk et al. (2010) in order to assess the validity of the authors' approach. Then, the authors present a series of numerical results related to the piezo-aeroelastic behavior of a vertical array of two harvesters.

5.1. Validation of the numerical model

Using the present piezo-aeroelastic model, the authors obtained the flutter speed and the piezoelectric response (pitch angle, plunge displacement, and voltage) generated by numerical simulations and compared them with analytical and experimental data reported by Erturk et al. (2010). The experiment they conducted consists of an airfoil connected to the ground through four steel beams, of which two have two PZT-5A piezoceramic patches attached close to the fixed ends in a

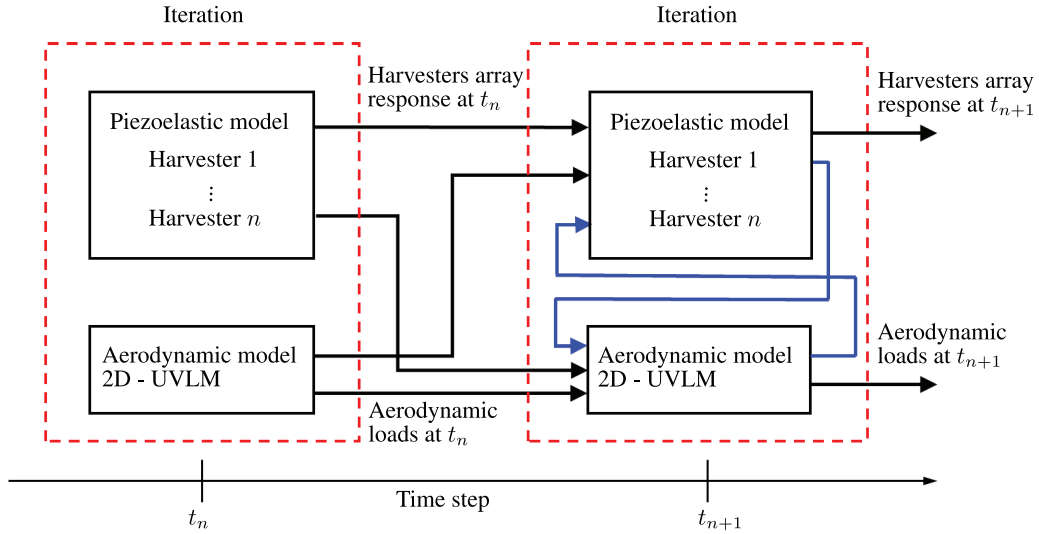


Figure 6. Simulation framework: coupling scheme between the 2D UVLM and the piezoelectric model. Source: Adapted from Roccia et al. (2017).

Table 2. System parameter data.

Parameter	Value
m	1.7799 kg/m
m_f	2.8425 kg/m
I_p	7.06445×10^{-3} kgm
b	0.125 m
x_θ	0.260
l	0.5 m
k_h	4.6808×10^3 N/m ²
k_θ	1.67540 N
d_h	9.6110×10^{-1} Ns/m ²
d_θ	1.32504×10^{-2} Ns
R	100 k Ω

symmetrical configuration. For their analytical model, they estimated the electromechanical coupling term as $\lambda = 1.55$ mN/V (Erturk and Inman, 2009). The equivalence capacitance value was provided by the

manufacturer, $C^{eq} = 120$ nF. The rest of the system parameters are presented in Table 2.

Both the size of the aerodynamic mesh and the consistent time step for the numerical integration procedure were determined by means of a convergence analysis (influence of the panel density on the flutter speed). These results are presented in Table 3. It should be noted that the simulation time step of an aeroelastic run mainly depends on the density of panels in the aerodynamic mesh. In Table 4, the authors present a summary of the computational costs for the numerical cases stated in Table 3.

As it can be observed from Table 3, the determined flutter speed approximates well the analytical value predicted by Erturk et al. (2010) as the aerodynamic mesh becomes denser. For 30 elements, the numerical model predicts a flutter speed of 9.451 m/s, which underestimates the analytical value of 9.56 m/s by 1.14%. Moreover, the relative percent error in the flutter speed

Table 3. Convergence analysis.

Density of the aerodynamic mesh	Flutter onset velocity (m/s)	Normalized plunge amplitude	Normalized pitch amplitude $\bar{\theta}/\bar{h}$ ($^\circ$ /mm)	Normalized voltage amplitude \bar{V}/\bar{h} (V/mm)	Maximum power amplitude \bar{P}/\bar{h}^2 (mW/mm ²)
Experimental ^a	9.30	1.000	0.55	4.27	0.182835
Analytical ^a	9.56	1.000	0.56	4.67	–
10 panels	9.055	1.000	0.565656	4.682675	0.219288
20 panels	9.352	1.000	0.559435	4.671655	0.218240
30 panels	9.451	1.000	0.557263	4.667887	0.217876
40 panels	9.5	1.000	0.556163	4.666002	0.217666
50 panels	9.53	1.000	0.555494	4.664844	0.217571
60 panels	9.55	1.000	0.555044	4.664059	0.217509

^aExperimental and analytical data reported by Erturk et al. (2010). Experimental plunge amplitude $\bar{h} = 7.65$ mm and analytical plunge amplitude $\bar{h} = 1.00$ mm.

Table 4. Computational cost for different aerodynamic meshes.

Mesh	Number of time steps	Time step Δt	Cost (s)
10	5000	2.761×10^{-3}	29
20	10,000	8.818×10^{-4}	196
30	13,700	8.815×10^{-4}	481
40	18,200	6.592×10^{-4}	1066
50	19,000	5.246×10^{-4}	1331
60	23,000	4.363×10^{-4}	2201

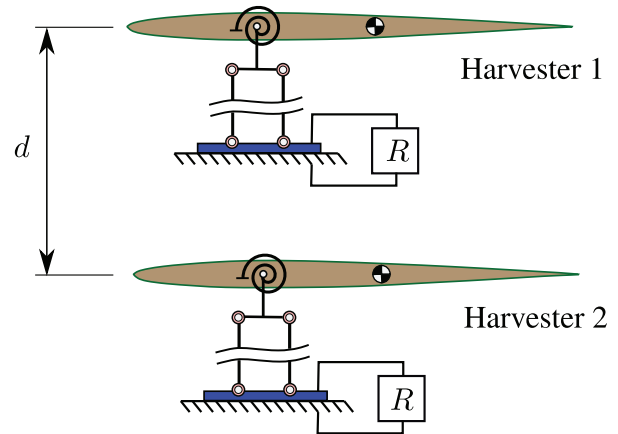
when 60 elements are used is reduced to 0.1%. However, the computational cost is increased from 481 s (approximately 8 min) to 2201 s (approximately 36 min). As previously mentioned, wake convection is the most expensive part of the authors' numerical approach, that is, double the paneling from 30 to 60 implies reducing the time step (almost by half), which in turn means more vortices within the wake. On this basis, an aerodynamic mesh consisting of 30 elements is found to provide an excellent trade-off between precision and computational cost. Henceforth, 30 elements are used for all of the numerical simulations reported in the rest of the article.

When the flutter speed predicted by the current model is compared against the experimental data, the predicted value is found to be an overestimate of the experimental flutter measurement of 9.30 m/s by 1.60%. As mentioned by Erturk and collaborators, the differences found between the analytical/numerical predictions and experimental data can be attributed, at first, to the 2D representation of a clearly 3D problem. The wing used by Erturk et al. has a constant-chord wing $2b$ and span l , thus having a relatively low-to-moderate aspect ratio $AR = l/2b = 2$. Therefore, the wing tip vortices can significantly affect the flow field around the wing, and consequently, the aerodynamic loads.

5.2. Case study

In this section, the authors present a comprehensive study of the flutter onset velocity and electric output power for an array of two vertically distributed harvesters. Both piezoelectric and structural data used here are the same as those used by Erturk et al. (2010). It should be stressed that the optimal resistance value R calculated for a single harvester is not necessarily the optimum value for the array of harvesters like the one proposed in this study. The flutter speed for the harvester array (hereafter denoted as V_F^A) was computed for several separation values between harvesters, ranging from $d = b$ to $d = 20b$ (see Figure 7).

First, the authors study how the flutter speed for the harvester system changes as the separation d is increased. In order to quantify this change and to

**Figure 7.** Vertical distribution of two harvesters separated by distance d .

define favorable/unfavorable zones, the authors adopt a reference speed of $V_F^{ref} = 9.451$ m/s, which corresponds to the flutter speed of a single harvester in isolation. It is well-known that when the wind speed is below the flutter speed, all oscillations in an aeronautical system will be damped with time. Conversely, wind speeds at, or above, the flutter speed will produce self-sustaining oscillations in the system, which, in the case of harvesting energy devices, means a sustained extraction of energy. On this basis, an important design criterion for future generations of power harvester arrangements will require making the onset flutter speed as low as possible. This feature will allow the harvester system to operate in a wide range of free-stream velocities.

As it can be observed in Figure 8, when the distance between harvesters is small enough ($b/d < 3$), the flutter speed for the two-harvester system is reduced below the reference speed V_F^{ref} (favorable zone). On the contrary, for values $b/d > 3$, the flutter speed V_F^A increases slightly above V_F^{ref} , reaching a maximum around $b/d = 5$ (unfavorable zone). Beyond $d/b = 5$, V_F^A approaches the reference speed, which means that each harvester behaves in isolation, or like a single harvester. This behavior can be explained from an aerodynamic point of view since the aerodynamic interaction between harvesters is attenuated as the distance between them is increased; therefore, the aeroelastic behavior of each harvester will not depend anymore on the remaining airfoils and their wakes.

In Figure 9, the authors show the variations of voltage-to-plunge, pitch-to-plunge, and mean electric power-to-plunge with respect to the dimensionless distance d/b . It should be noted that the curves presented in Figure 9 correspond to one harvester; hence, the total output power for the array is twice the value reported in Figure 9(c). Furthermore, the power is calculated from the voltage according to

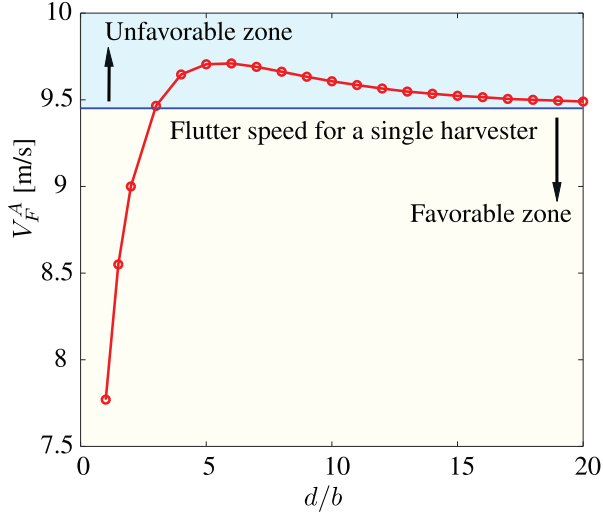


Figure 8. Flutter speed for the harvester array as function of the dimensionless distance d/b .

$$P = \frac{V^2}{R} \quad (17)$$

The mean output power \hat{P}_m per unit length squared, at flutter speed, presents a relatively large value for $d/b = 1$, but is still less than the value produced by an isolated harvester. From this value, \hat{P}_m decreases to a minimum around $d/b = 3$ and then increases slowly approaching the power value produced by a single harvester in isolation (see Figure 9(c)). At first, the introduction of a second harvester into the system produces the undesired effect of decreasing the output power. However, the reduction produced is scarcely noticeable, being only 1.3% for $d/b = 1$. However, a new perspective emerges when the information provided by Figure 8 is taken into account. Particularly, for two harvesters separated by $d/b = 1$, the flutter onset velocity decreases to 7.78 m/s (about 18% lower than the flutter speed for a single harvester). This fact highlights the tremendous advantage of generating energy, at low wind speeds, by means of an arrangement of harvesters.

Unlike the voltage and power, the pitch has a monotonic decay from 0.611 °/mm until it becomes asymptotic to the value of 0.557 °/mm when the separation between harvesters is large enough. According to Figure 9(b), the maximum pitching amplitude is obtained when the distance between airfoils is the smallest possible, which here is $d/b = 1$. Recalling that the velocity field induced by a VP on an arbitrary point P in space decays as P moves away from the vortex (see equation (7)), it might be concluded that the most significant aerodynamic interaction occurs for small values of d/b . This finding suggests that, for a vertical configuration of harvesters at flutter speed, small separations imply higher aerodynamic interactions, which in turn imply larger pitch oscillations.

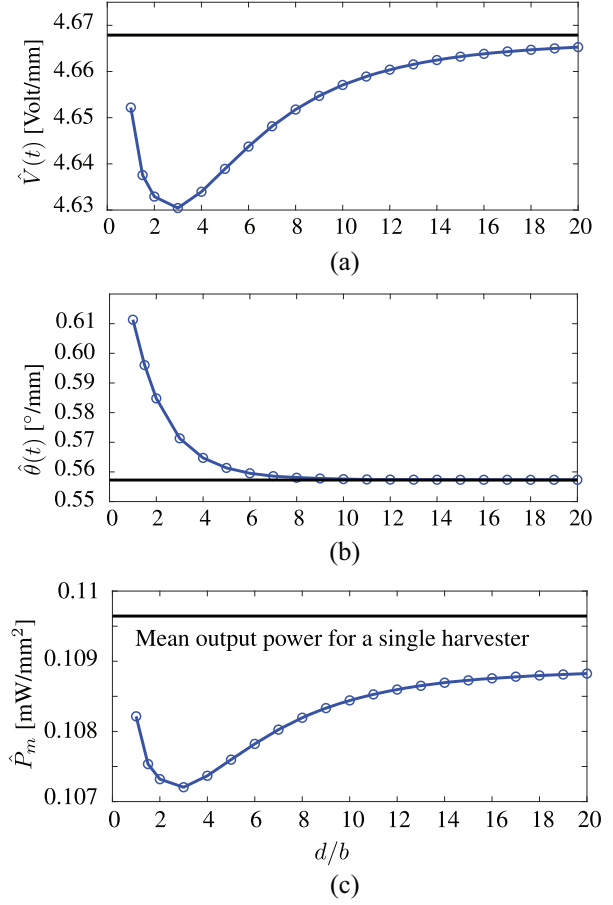


Figure 9. Normalized voltage \hat{V} , pitch $\hat{\theta}$, and mean output power \hat{P}_m for one harvester within the array as function of the dimensionless distance d/b . (a) Normalized voltage, (b) Normalized pitch angle, (c) Normalized mean output power.

Despite the lack of structural nonlinearities, the aerodynamic interaction between relatively close airfoils is enough to produce nonlinear responses in post-flutter scenarios, such as limit cycle oscillations (LCOs). In Figure 10, the authors show the Hopf bifurcation associated with the pitching motion for $d/b = 1$. As can be gathered, this bifurcation is supercritical, and hence, the LCOs are born above the flutter speed. The pitch-LCO amplitude initially increases, reaches a maximum at point P_4 , and then begins to decrease. This trend was found to be similar to the results reported by Abdelkefi et al. (2012), who also pointed out the possibility of periodic motions with large periods or quasiperiodic motions.

Further increments of the wind speed beyond point P_4 result in a substantial change in the nature of the pitch signal. In terms of the frequency spectrum, the signal changes from an almost pure sinusoidal signal to a sideband one (points Q_1 and Q_2 in Figure 11(c)). This phenomenon is also observed as a shape modification on the pitch-LCO phase portrait, going from an ellipse (point P_3 in Figure 10) to a curve that crosses itself

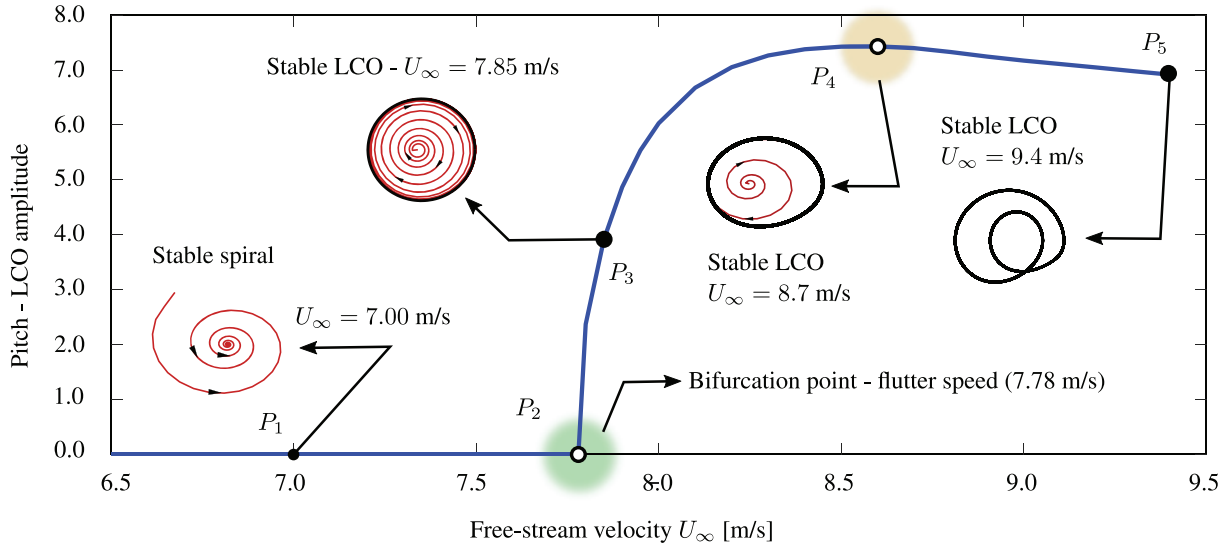


Figure 10. Pitching LCO amplitude versus free-stream speed for $d/b = 1$. A supercritical Hopf bifurcation occurs at 7.78 m/s.

(point P_5 in Figure 10). As an example, in Figure 11(d), the phase portrait is shown for a wind speed of 9.4 m/s, where the blue portion corresponds to the transient window (see Figure 11(a)) and the black portion represents the LCO once the steady state solution is reached (Figure 11(b)). In this work, the LCO amplitudes were determined by means of a standard least-squares fitting procedure for ellipses (see Figure 11(e); Rosin, 1993). Similar behavior was found for the plunge response.

According to the intuitive definition of Wiggins (1988) and Nayfeh and Balachandran (1995), a quasi-periodic orbit is just a two-frequency solution of the ODE, where the two frequencies are incommensurate. In this sense, the results presented above do not show any evidence of quasiperiodic motion since the ratio between the sideband frequencies and the fundamental one is 2 and $3/2$, respectively.

In addition, point P_4 , where the pitch bifurcation curve reaches a maximum, can potentially be a candidate for a secondary Hopf bifurcation (SHB) location. Here, it was not possible to find another branch leaving this point (by varying the initial conditions (ICs)), possibly due to the lack of structural nonlinearities. Heuristically speaking, another signature of an SHB occurrence is related to the detection of a jump phenomenon in the fundamental frequency as the wind speed is increased. According to Liu and Dowell (2004), for motions before an SHB point, the fundamental frequency value keeps decreasing as the flow velocity increases, while for motions after the SHB, this frequency value remains unchanged. In this work, both the pitching and plunging as well as the voltage always show a decreasing trend in the fundamental frequency value as the wind speed increases, exhibiting a change in the slope when point P_4 is reached.

In Figure 12, the authors show the supercritical Hopf bifurcation for the voltage and mean output

power P_m . After the first Hopf bifurcation, the voltage and output power reach a maximum at point A and then begin to decrease. From an energy viewpoint, with a harvester array working in a post-critical scenario, one can have a considerable improvement in the collected energy. Specifically, for $d/b = 1$, the maximum mean output power is obtained when $V_\infty = 8.7$ m/s, which represents a 92.05% of the necessary speed to reach flutter in an isolated harvester. In this configuration, each piezoelectric airfoil provides a P_m of 63.049 or 126.0980 mW taking into account both harvesters.

As the separation between harvesters increases, the system presents a similar behavior as described above. Particularly, for $d/b = 2$, the pitching, plunging, and voltage response all reveal a first supercritical Hopf bifurcation at $V_\infty = 9.00$ m/s, after which these responses reach their maximum values (around $V_\infty = 10.5$ m/s), before they start to decrease. For this configuration, the maximum mean output power is 320.277 mW for one harvester and, as before, such a point can be recognized as a potential SHB.

Finally, in Figure 13, the authors show the temporal evolution for the harvester arrangement studied above ($d/b = 1$ and $V_\infty = 9.4$ m/s). The set of ICs is the following: $\mathbf{q}_1(0) = \mathbf{0}$, $\dot{\mathbf{q}}_1(0) = \mathbf{0}$, $\mathbf{q}_2(0) = (-1.0 \times 10^{-3}, 0, 0)^T$, and $\dot{\mathbf{q}}_2(0) = \mathbf{0}$. From Figure 13(a) to (g), it is noted that the flow field around the system is symmetrized as time increases. This feature was found for all simulated cases. Moreover, symmetrization of the flow was found whenever an even number of harvesters is used (always in a vertical distribution). On the contrary, for an odd number of harvesters, the flow pattern is dependent on the ICs. To probe this further, the authors consider three harvesters, in a vertical configuration, uniformly distributed, and with ICs given by: $\mathbf{q}_1 = (0, \theta_0, 0)^T$, $\mathbf{q}_2 = (0, 0, 0)^T$, and $\mathbf{q}_3 = (0, -\theta_0, 0)^T$ along with all velocities set to zero (see Figure 14). Under these assumptions,

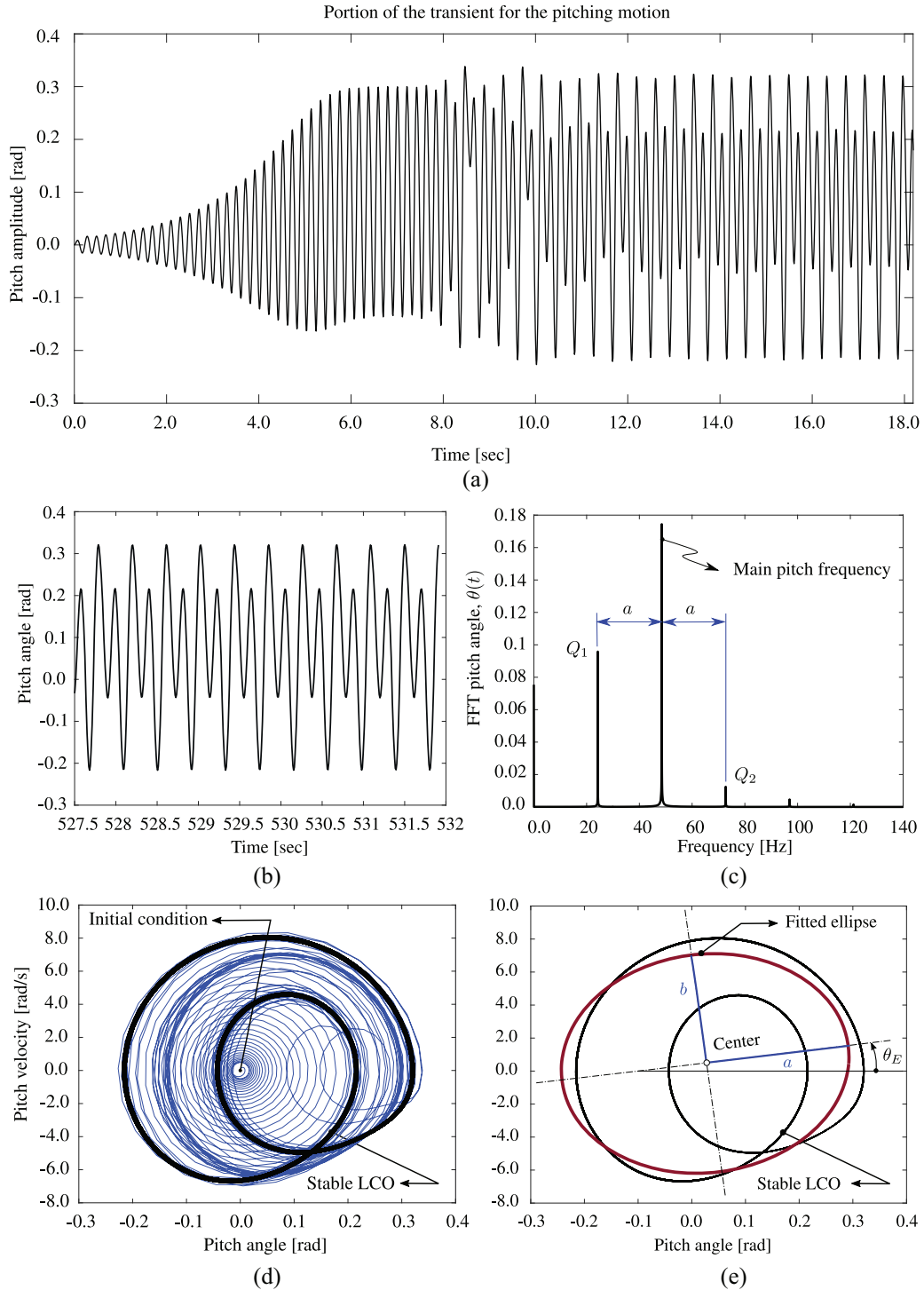


Figure 11. Time series, FFT, and phase portrait for pitching motion at $U_\infty = 9.4$ m/s (point P_2 in Figure 10) and $d/b = 1$: (a) portion of the transient for the pitching motion, (b) pitching at steady state, (c) FFT of the pitch angle, (d) phase portrait corresponding to (a), and (e) fitted ellipse to approximate the LCO showed in (d).

there is an unstable solution where the harvester located in between does not move, and therefore, the resulting flow field around the system is symmetrical. Of course, any numerical disturbance (e.g. roundoff errors) will break the flow symmetry. Any other combination of ICs will produce different flow field patterns. Regardless of

whether the flow around the system symmetrizes or not, a wake synchronization can also be observed. This phenomenon of “synchronization” between harvesters is exclusively due to the aerodynamic interactions between them and needs to be studied in more detail in order to elucidate the effect on the production of electric power.

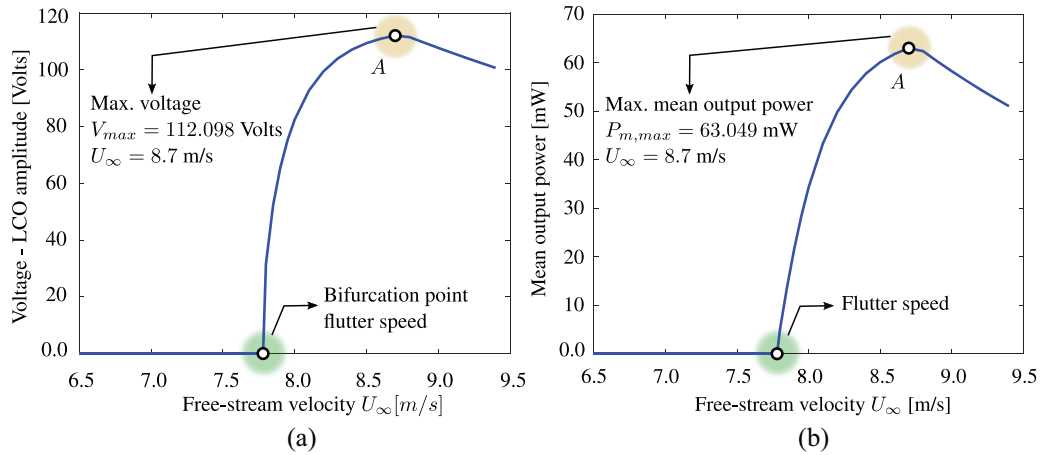


Figure 12. Variation of the voltage and harvested power with respect to the free-stream speed for $d/b = 1$: (a) voltage – LCO amplitude and (b) mean output power.

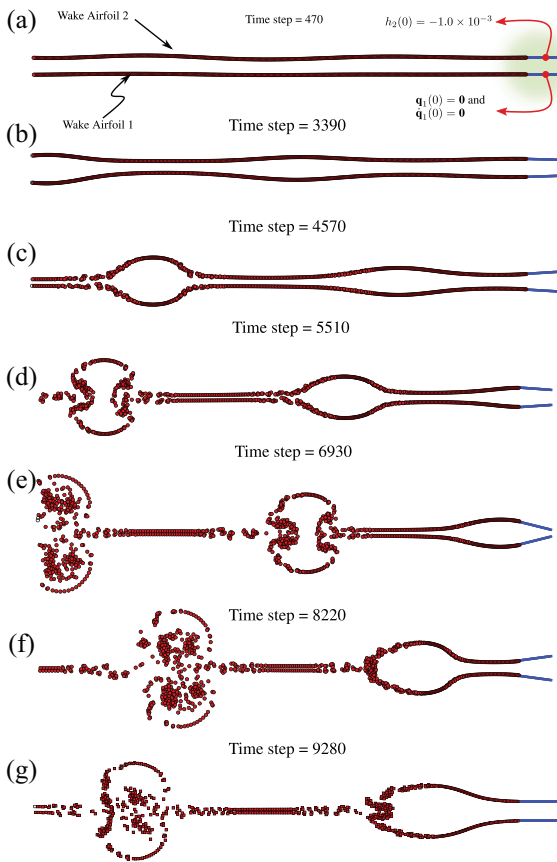


Figure 13. Wake evolution for $d/b = 1$ and $V_\infty = 9.4$ m/s. (a) flow pattern at time step 470, (b) flow pattern at time step 3390, (c) flow pattern at time step 4570, (d) flow pattern at time step 5510, (e) flow pattern at time step 6930, (f) flow pattern at time step 8220, and (g) flow pattern at time step 9280.

Despite the attractive findings presented above, it is necessary to conduct more research in this direction to fully understand the piezo-aeroelastic behavior of harvester arrays and how to optimize energy extraction. As

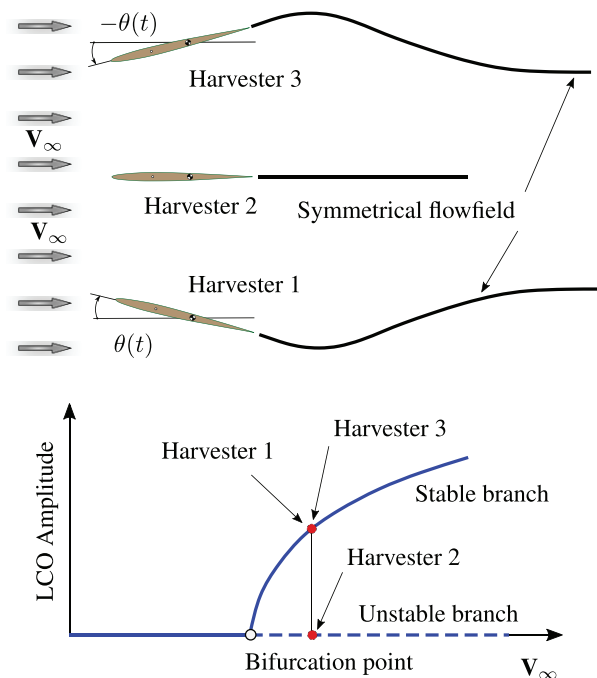


Figure 14. Descriptive scheme of a possible symmetric flow field for three harvesters.

enhancements, the current aerodynamic model can be extended by incorporating a growth core-vortex scheme in order to handle tandem configurations of harvesters (Bhagwat and Leishman, 2002; Rocca et al., 2018). In addition, the use of the fast multipole method to rapidly compute the velocity contribution from the time-varying wakes will also be desirable (Kebbie-Anthony et al., 2019). Regarding the structural model, one can conclude that a significant limitation is the lack of consideration of nonlinearities, which are necessary to conduct more detailed studies on the dynamic behavior of the piezo-aeroelastic system, such as detection of quasiperiodic motions, intermittence, determination of SHB points, and chaos.

6. Conclusion

In this article, a simulation framework for studying the piezo-aeroelastic behavior of an arrangement of harvesters has been presented. The subsystem involving the piezoelastic model has been successfully coupled in a strong way with the subsystem that models the aerodynamics, which is based on the UVLM. The numerical integration of the EoMs was performed in the time domain using the Hamming's fourth-order predictor–corrector method. The computational model was validated by comparing the results against analytical and experimental data reported in the literature. Specifically, the flutter speed predicted by the current model was found to be in excellent agreement with the data obtained from the literature.

Some important inferences can be drawn from the preceding sections. The findings help to better understand the underlying physics associated with the piezo-aeroelastic behavior of arrangements of harvesters, whose complexity is well-accepted but at the same time not well-understood. The use of an array of two vertically distributed harvesters was found to have an interesting influence on the onset flutter speed. Specifically, when the distance between harvesters is small enough, the flutter speed for the array is reduced below the flutter speed for one harvester in isolation (reference speed). As the separation between them increases, the flutter speed also increases, reaching a maximum, and then approaching the reference speed. This behavior allows one to define two regions: a favorable zone, where the system of harvesters can generate power at low wind speeds; and an unfavorable zone, where the “array” behaves like two harvesters working in isolation.

Although the simulation framework presented does not take into account any structural nonlinearity, the aerodynamic interaction between relatively close airfoils is enough to produce nonlinear responses at post-flutter scenarios, such as LCOs. In fact, the post-critical behavior is characterized by a supercritical Hopf bifurcation, from which the mean output power increases until a maximum is reached, and then begins to decrease. This result provides a glimpse into a new generation of self-configuring energy harvesting devices that can be used to maximize the generated power for a wide range of wind speeds. In the light of this assertion, and for the case analyzed in this work, the use of two harvesters, working at a post-critical scenario, allows the output power to be increased at low wind speeds.

These results show that the present approach is indeed capable of predicting, with notable accuracy, the piezoelastic response, unsteady aerodynamics, and nonlinear dynamic behavior of an array of harvesters. The computational modeling's promising features warrant further investigations in this direction. Although

the proposed model can serve as a good starting point to improve the understanding of flutter-based harvester devices, more research will be necessary. In the future, the current methodology will be enhanced by means of the expansion of the presented ideas, for example, the inclusion of a growth core-vortex scheme and the inclusion of a general model that take into account the dynamics of detachment and reattachment. Moreover, the piezoelastic model will be improved by adding structural nonlinearities; features are strictly necessary to quantify the possibility of subcritical behavior, hysteresis, quasiperiodic motions, intermittence, and the presence of chaos. In addition, it is intended to develop a simulation environment, in which one can couple the piezo-aeroelastic model presented here with an optimization code in order to investigate the best distribution of harvesters for energy production.

Acknowledgements

The authors gratefully acknowledge the partial support received from the Consejo Nacional de Investigaciones Científicas y Técnicas (CONICET), Argentina. In addition, the authors thank the Area de Tecnologías de la Información (ATI), Engineering School, Universidad Nacional de Río Cuarto, and CSA. Ariel R.C. Flores for his technical support in the area of computing technologies. Support received through the Minta Martin Professorship at the University of Maryland, College Park, is also gratefully acknowledged.

Declaration of conflicting interests


The author(s) declared no potential conflicts of interest with respect to the research, authorship, and/or publication of this article.

Funding

The author(s) received no financial support for the research, authorship, and/or publication of this article.

ORCID iDs

Bruno A Roccia  <https://orcid.org/0000-0001-6403-2739>

Luis R Ceballos  <https://orcid.org/0000-0002-4083-6692>

References

- Abdelkefi A, Nayfeh AH and Hajj MR (2012) Design of piezoaeroelastic energy harvesters. *Nonlinear Dynamics* 68: 519–530.
- Bae JS and Inman DJ (2014) Aeroelastic characteristics of linear and nonlinear piezo-aeroelastic energy harvester. *Journal of Intelligent Material Systems and Structures* 25: 401–416.
- Bao C, Dai Y, Wang P, et al. (2019) A piezoelectric energy harvesting scheme based on stall flutter of airfoil section. *European Journal of Mechanics: B/Fluids* 75: 119–132.
- Bhagwat MJ and Leishman JG (2002) Generalized viscous vortex core models for application to free-vortex wake and

- aeroacoustic calculations. In: *American helicopter society 58th annual forum proceedings*, Montreal, QC, Canada, 11–13 June.
- Bryant M and Garcia E (2009) Development of an aeroelastic vibration power harvester. In: *Proceeding of the SPIE sixteenth international symposium on smart structures and materials & nondestructive evaluation and health monitoring*, vol. 7288, San Diego, CA, 8–12 March, p. 728812. Bellingham, WA: SPIE.
- Bryant M and Garcia E (2011) Modeling and testing of a novel aeroelastic flutter energy harvester. *Journal of Vibration and Acoustics* 133: 011010.
- Bryant M, Fang A and Garcia E (2010) Self-powered smart blade: helicopter blade energy harvesting. In: *Proceedings of the SPIE 7643: Active and passive smart structures and integrated systems*, vol. 7643, San Diego, CA, 7–11 March, pp. 171–179. Bellingham, WA: SPIE.
- Bryant M, Mahtani RL and Garcia E (2012) Wake synergies enhance performance in aeroelastic vibration energy harvesting. *Journal of Intelligent Material Systems and Structures* 23: 1131–1141.
- Carnahan B, Luther HA and Wilkes JO (1969) *Applied Numerical Methods*. New York: Wiley, pp. 390–392.
- Deivasigamani A, McCarthy JM, John SJ, et al. (2014) Proximity effects of piezoelectric energy harvesters in fluid flow. In: *29th congress of the international council of the aeronautical sciences*, St. Petersburg, Russia, 7–12 September.
- Dias J, Marqui CD and Erturk A (2014) Three-degree-of-freedom hybrid piezoelectric-inductive aeroelastic energy harvester exploiting a control surface. *AIAA Journal* 53: 394–404.
- Doare O and Michelin S (2011) Piezoelectric coupling in energy harvesting fluttering flexible plates: linear stability analysis and conversion efficiency. *Journal of Fluids and Structures* 27: 1357–1375.
- Elahi H, Eugeni M and Gaudenzi P (2019) Design and performance evaluation of a piezoelectric aeroelastic energy harvester based on the limit cycle oscillation phenomenon. *Acta Astronautica* 157: 233–240.
- Erturk A and Inman DJ (2009) An experimentally validated bimorph cantilever model for piezoelectric energy harvesting from base excitations. *Smart Materials and Structures* 18: 025009.
- Erturk A, Vieira WGR, Marqui CD, et al. (2010) On the energy harvesting potential of piezoaeroelastic systems. *Applied Physics Letters* 96: 184103.
- Fitzgerald T, Valdez MF, Vanella L, et al. (2011) Flexible flapping systems: computational investigations into fluid-structure interactions. *The Aeronautical Journal* 115(1172): 593–604.
- Hodges DH and Pierce GA (2011) *Introduction to Structural Dynamics and Aeroelasticity*. 2nd ed. New York: Cambridge University Press.
- Katz J and Plotkin A (2001) *Low-Speed Aerodynamics*. 2nd ed. New York: Cambridge University Press.
- Kebbie-Anthony A, Gumerov NA, Preidikman S, et al. (2019) Fast multipole accelerated unsteady vortex lattice method based computations. *Journal of Aerospace Information Systems* 16(6): 237–248.
- Konstadinopoulos P, Mook DT and Nayfeh AH (1981) A numerical method for general unsteady aerodynamics. In: *AIAA atmospheric flight mechanics conference*, Albuquerque, NM, 19–21 August.
- Krasny R (1987) Computation of vortex sheet roll-up in the Trefftz plane. *Journal of Fluid Mechanics* 184: 123–155.
- Liu L and Dowell EH (2004) The secondary bifurcation of an aeroelastic airfoil motion: effect of high harmonics. *Non-linear Dynamics* 37: 31–49.
- McCarthy JM, Deivasigamani A, Watkins S, et al. (2014) On the visualisation of flow structures downstream of fluttering piezoelectric energy harvesters in a tandem configuration. *Experimental Thermal and Fluid Science* 57: 407–419.
- McCarthy JM, Watkins S, Deivasigamani A, et al. (2016) Fluttering energy harvesters in the wind: a review. *Journal of Sound and Vibration* 361: 355–377.
- Nayfeh A and Balachandran B (1995) *Applied Nonlinear Dynamics: Analytical, Computational, and Experimental Methods*. New York: Wiley.
- Peters DA (1985) Toward a unified lift model for use in helicopter rotor blade stability analyses. *Journal of the American Helicopter Society* 30(3): 32–43.
- Preidikman S (1998) *Numerical simulations of interactions among aerodynamics, structural dynamics, and control systems*. PhD Dissertation, Department of Engineering Science and Mechanics, Virginia Polytechnic Institute and State University, Blacksburg, VA.
- Preidikman S and Mook DT (2000) Time domain simulations of linear and nonlinear aeroelastic behaviour. *Journal of Vibrations and Control* 6(8): 1135–1175.
- Preidikman S, Roccia BA, Verstraete ML, et al. (2017) Chapter 1: Computational aeroelasticity of flying robots with flexible wings. In: Lopez Mejia OD and Escobar Gomez JA (eds) *Aerial Robots*. London: Intech, pp. 3–30.
- Roccia BA, Preidikman S and Balachandran B (2017) Computational dynamics of flapping wings in hover flight: a co-simulation strategy. *AIAA Journal* 55(6): 1806–1822.
- Roccia BA, Preidikman S, Massa JC, et al. (2013) Modified unsteady vortex-lattice method to study flapping wings in hover flight. *AIAA Journal* 51(11): 2628–2642.
- Roccia BA, Verstraete ML, Dimitriadis G, et al. (2018) Unsteady aerodynamics and nonlinear dynamics of free-falling rotating seeds. In: *Proceedings of ISMA 2018 and USD 2018*, Leuven, 17–19 September, pp. 2615–2630. Leuven: Katholieke Universiteit Leuven.
- Rosin PL (1993) A note on the least squares fitting of ellipses. *Pattern Recognition Letters* 14(10): 799–808.
- Rostami AB and Armandei M (2017) Renewable energy harvesting by vortex-induced motions: review and benchmarking of technologies. *Renewable and Sustainable Energy Reviews* 70: 193–214.
- Sousa VC, Anic é zio M de M, De Marqui C, et al. (2011) Enhanced aeroelastic energy harvesting by exploiting combined nonlinearities: theory and experiment. *Smart Materials and Structures* 20: 094007.
- Verstraete ML, Preidikman S, Roccia BA, et al. (2015) A numerical model to study the nonlinear and unsteady aerodynamics on a bioinspired morphing wing concepts. *International Journal of Micro Air Vehicles* 7(3): 327–345.
- Wiggins S (1988) *Global Bifurcations and Chaos*. New York: Springer-Verlag.
- Wu Y, Li D, Xiang J, et al. (2017) Piezoaeroelastic energy harvesting based on an airfoil with double plunge degrees of freedom: modeling and numerical analysis. *Journal of Fluids and Structures* 74: 111–129.